catalysts

MDPI

Article

Structure-Dependent Photocatalytic Performance of $BiOBr_xI_{1-x}$ Nanoplate Solid Solutions

Huan-Yan Xu *, Xu Han, Qu Tan, Xiu-Lan He and Shu-Yan Qi

School of Materials Science and Engineering, Harbin University of Science and Technology, Harbin 150040, China; h458273079@sina.com (X.H.); tanqu2000@163.com (Q.T.); hexiulan1973@126.com (X.-L.H.); qishuyan10@163.com (S.-Y.Q.)

* Correspondence: xhy7587@aliyun.com; Tel.: +86-451-8639-2501

Academic Editors: Giuseppe Marcì and Elisa I. García-López

Received: 19 April 2017; Accepted: 9 May 2017; Published: 13 May 2017

Abstract: $BiOX_xY_{1-x}$ (X, Y = Cl, Br, and I) solid solutions have been regarded as promising photocatalysts attributed to their unique layered structure, tunable band structure, and chemical and optical stability. In this study, $BiOBr_xI_{1-x}$ nanoplate solid solutions with a high exposure of {001} crystal facets were prepared by a facile alcoholysis method at room temperature and atmospheric pressure. X-ray diffraction (XRD) peaks exhibited a slight shift to lower diffraction angle with the increase of I content in $BiOBr_xI_{1-x}$ samples, which resulted in a gradual increase in their cell parameters. Field emission scanning electron microscopy (FESEM) and transmission electron microscope (TEM) images revealed that $BiOBr_xI_{1-x}$ samples exhibited 2D plate-like structure with the in-plane wrinkles. The regular changes in optical absorption threshold and E_g value seen in UV-vis diffuse reflectance spectra (UV-vis DRS) indicated that the optical absorption property and band structure could be modulated by the formation of $BiOBr_xI_{1-x}$ solid solutions. The photocatalytic degradation of active dye Rhodamine B (RhB) over $BiOBr_xI_{1-x}$ solid solutions showed that $BiOBr_{0.75}I_{0.25}$ had the best photocatalytic activity. The RhB photodegradation processes followed a pseudo-first-order kinetic model. The synergistic effect of structural factors (including amount of exposed {001} facets, interlayer spacing of (001) plane, and energy-level position of the valence band) determined the photocatalytic performance of $BiOBr_xI_{1-x}$ solid solutions.

Keywords: bismuth oxyhalide; photocatalysis; exposed facets; interlayer spacing; band structure

1. Introduction

Heterogeneous photocatalysis processes have gained more attention in recent decades, attributed to their diverse applications in many fields, such as wastewater remediation, air purification, disinfection, hydrogen production, and catalysis of organic syntheses [1–6]. The performance of a photocatalyst mainly depends on two factors, namely band gap and redox potential. The former requires that the energy of available photons must be larger than the band gap (E_g) of the photocatalyst; and the latter demands that the redox potential of reactants must be situated between the conduction band minimum (CBM) and the valence band maximum (VBM) of the photocatalyst [7]. TiO_2 is a well-known semiconductor photocatalyst. However, the band gaps of rutile and anatase are 3.0 eV and 3.2 eV, respectively, which indicate that they only can be excited by ultraviolet light (about 4% of total solar energy) [8,9]. In order to realize the excitation of TiO_2 by sunlight, many efforts have been made to introduce metal or non-metal impurities into TiO_2 structure, which can form the acceptor or donor states in TiO_2 band gap [10]. Moreover, numerous novel semiconductors with narrow band gap have been developed to improve the harvesting ability across the visible region, including perovskites, organic metal halides, non-noble metal-based compounds, and transition metal oxides and sulfides [11–20].

Bismuth oxyhalide (BiOX, X = Cl, Br, and I) semiconductor materials have been regarded as promising photocatalysts because they have a unique layered structure, suitable band structure, and chemical and optical stability [21]. Their crystal structures belong to the tetragonal space group $P4/nmm$ and are defined as a matlockite (PbFCl-type) structure with the atomic positions: Bi, $00u$,$\frac{1}{2}$ $\frac{1}{2}$ $\overline{u}$; X, $00v$, $\frac{1}{2}$ $\frac{1}{2}$ $\overline{v}$; O, $\frac{1}{2}$ 00, 0 $\frac{1}{2}$ 0 [22,23]. The typical layered structure of bismuth oxyhalides is constituted by $[Bi_2O_2]^{2+}$ layers intercalated with double layers of halogen ions. The atoms within $[Bi_2O_2]^{2+}$ layers interact each other via covalent bonds, whereas the stack along the *c*-axis of [X] layers is realized by van der Waals force [24,25]. This layered structure facilitates the internal electric fields (IEF) that can promote the effective separation of the photogenerated electron-hole pairs [26]. The band gaps of BiOCl, BiOBr, and BiOI are 3.22 eV, 2.64 eV, and 1.77 eV, respectively. This decrease in the band gap with the electronegativity of X decreasing reflects the electronic structures of BiOX, where the CBM and VBM are dominated by the Bi 6p and X np orbitals, respectively [27]. Accordingly, the light response of BiOX can be modulated from UV to visible light by changing the halogen ions. Because BiOCl, BiOBr and BiOI have the same layered structure and atomic arrangement, other halogen atoms can be easy to incorporate into their lattice, consequently realizing the substitution of each other to form $BiOX_xY_{1-x}$ (X, Y = Cl, Br, and I) solid solutions [26]. The formation of solid solutions might be an ideal strategy to realize the continuous adjustment of the VBM energy levels. Up until now, a series of $BiOCl_xBr_{1-x}$ [26–31], $BiOCl_xI_{1-x}$ [32–35], and $BiOBr_xI_{1-x}$ [36–39] solid solutions have been obtained as a highly efficient photocatalyst with a tunable band gap and visible-light response. In addition, it has been reported that BiOX nanoplates with {001} facets exposure showed higher photocatalytic activity than those with {010} facets exposure, attributed to their better adsorption property, stronger IEF, and higher separation and transfer efficiency of photogenerated electron-hole pairs [24,30,40,41]. However, the exposure of a specific crystal facet for BiOX nanomaterials strongly depended on the pH value of their growth environment. Generally, the strong acid condition (such as pH = 1) was mandatory in the hydrothermal route for {001} facet-selective growth of BiOXs [24]. Hence, how to realize high {001} facets exposure in a facile and low-cost route still remains a challenging task for BiOXs, especially their solid solutions. Moreover, the formation of solid solutions can result in regular changes of crystal structure, band gap, and IEF of BiOXs and consequently affect their photocatalytic activities. The inherent correlation between crystal structure and enhanced photocatalytic activity of BiOX solid solutions still needs further insight and understanding.

In this study, $BiOBr_xI_{1-x}$ solid solutions were selected as the objectives of study and an alcoholysis method was developed to synthesize $BiOBr_xI_{1-x}$ nanoplates at room temperature and atmospheric pressure. In this route, a strong acid/alkaline environment was absolutely avoided to realize the high exposure of {001} crystal facets. Followed by the characterization analyses by XRD, FESEM, TEM, UV-vis DRS, energy dispersive spectra (EDS), and BET surface area analyzer, the obtained samples were arranged for the assessment of their photocatalytic activities under simulated sunlight irradiation using RhB as the target pollutant. Then, the atomic configuration, cell parameter, interlayer spacing, exposed facet, and energy band structure of $BiOBr_xI_{1-x}$ solid solutions were calculated and discussed with the aim to further understand structure-dependent enhanced photocatalytic activity of $BiOBr_xI_{1-x}$ nanoplate solid solutions.

2. Results and Discussion

2.1. Crystal Phase and Morphology of $BiOBr_xI_{1-x}$ Solid Solutions

The XRD results of $BiOBr_xI_{1-x}$ samples are presented in Figure 1, where it can be seen that all the diffraction peaks are sharp, indicating successful crystallization of $BiOBr_xI_{1-x}$ samples prepared by the alcoholysis route [42]. The two end-member samples, i.e., BiOBr and BiOI are in good accordance with JCPDS standard cards No. 78-348 and 73-2062, respectively. As expected, all the diffraction peaks present a slight shift to lower diffraction angle with the increase of I content in $BiOBr_xI_{1-x}$ samples. This phenomenon can be explained by the fact that after the substitution of smaller Br ions

(r_{Br} = 0.196 nm) by larger I ions (r_{Br} = 0.216 nm), the interlayer spacings expand. In the same way, the cell parameters of all the samples gradually increase with I content increasing, as listed in Table 1. These regular changes in XRD peaks and cell parameters as a function of I content strongly declare that the obtained $BiOBr_xI_{1-x}$ products belong to a group of solid solutions [27]. In addition, there are no other diffraction peaks of impurity, which implies that all the atoms entered into the crystal lattice and the stoichiometric value x in $BiOBr_xI_{1-x}$ was accurately determined by the initial proportion of Br and I sources in the preparation procedure [36,39]. The relative intensities of (001), (002), and (004) peaks gradually become stronger with increasing I content; on the contrary, that of (101) peak gradually weakens. Furthermore, in all the XRD patterns, the relative intensity of (001) peak is stronger than that of (101) peak, suggesting that the exposure percentage of {001} crystal facets is higher than that of {101} crystal facets in all the samples with highly preferred (001) orientation [43]. Thus, the as-prepared samples in this work can be determined as $BiOBr_xI_{1-x}$ solid solutions with high {001} facets exposure.

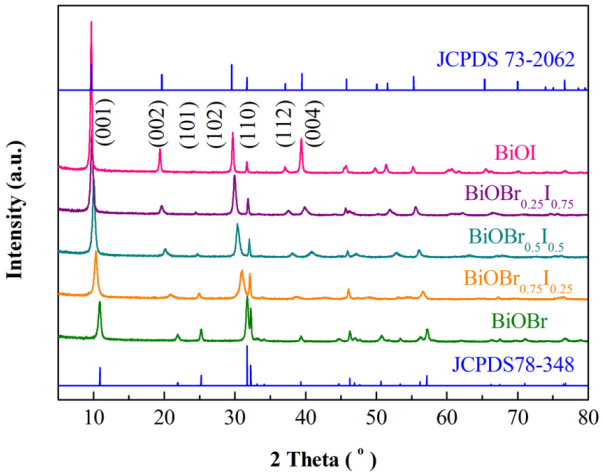

Figure 1. X-ray diffraction (XRD) patterns of $BiOBr_xI_{1-x}$ samples.

Table 1. Cell parameters and band structure calculations of $BiOBr_xI_{1-x}$ solid solutions, and reaction rate constants of photodegradation of Rhodamine B (RhB) over $BiOBr_xI_{1-x}$ samples.

Sample	*a* (Å)	*c* (Å)	Band Gap (eV)	χ (eV)	CBM (eV)	VBM (eV)	*k* (min^{-1})
BiOBr	3.9249	8.0954	2.86	6.45	0.52	3.38	−0.00834 (R^2 = 0.98302)
$BiOBr_{0.75}I_{0.25}$	3.9416	8.4286	2.17	6.39	0.81	2.98	−0.02864 (R^2 = 0.95625)
$BiOBr_{0.5}I_{0.5}$	3.9456	8.9083	2.06	6.33	0.80	2.86	−0.02401 (R^2 = 0.97219)
$BiOBr_{0.25}I_{0.75}$	3.9756	9.0603	1.97	6.27	0.79	2.76	−0.00878 (R^2 = 0.98838)
BiOI	3.9996	9.1509	1.87	6.21	0.78	2.65	−0.00194 (R^2 = 0.81574)

The morphological structure of $BiOBr_xI_{1-x}$ solid solutions was observed by FESEM and TEM, as displayed in Figures 2 and 3, respectively. In Figure 2, the FESEM images reveal that all of the $BiOBr_xI_{1-x}$ samples exhibit a 2D plate-like structure with a diameter of 0.2–1.0 μm and thickness of 40–60 nm. These nanoplates irregularly stack together without a specific architecture, such as microsphere or flower. EDS analysis indicates that typical $BiOBr_xI_{1-x}$ (x = 0.5) has the main elements Bi, O, Br, and I. Also, as expected, the atomic ratio of Br and I is approximate to 1. In the TEM images (Figure 3), 2D nanosheet structures of $BiOBr_xI_{1-x}$ samples can be clearly seen. These nanosheets are so thin that the overlayed shadow is visible. Moreover, the in-plane wrinkles of the nanosheets can be distinctly observed, which might be attributed to the existence of inner strain in the $BiOBr_xI_{1-x}$ structure. The inner strain can change the band structure and facilitate the charge separation, accordingly improving the photocatalytic activity of BiOX [44].

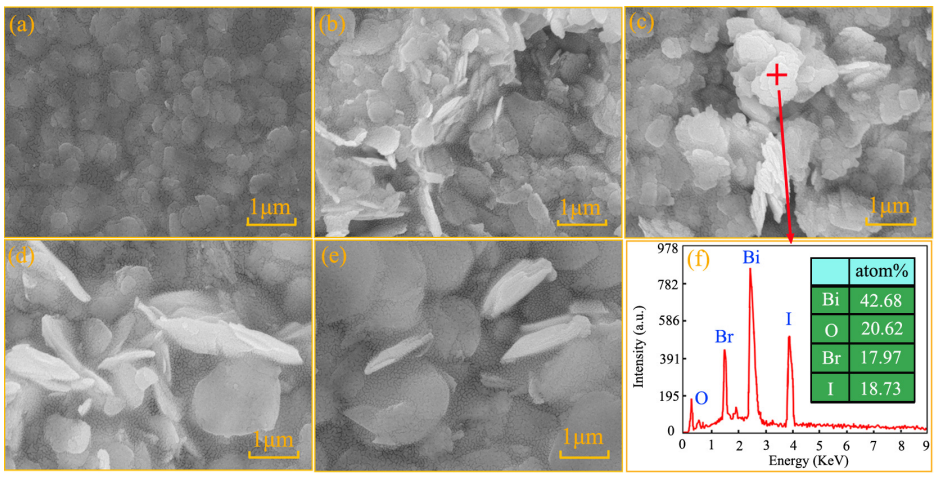

Figure 2. Field emission scanning electron microscopy (FESEM) images of (**a**) BiOBr, (**b**) $BiOBr_{0.75}I_{0.25}$, (**c**) $BiOBr_{0.5}I_{0.5}$, (**d**) $BiOBr_{0.25}I_{0.75}$, (**e**) BiOI; and EDS element analysis of (**f**) $BiOBr_{0.5}I_{0.5}$.

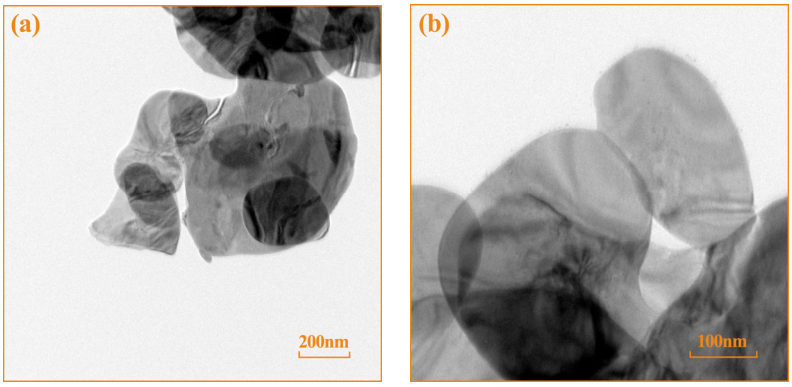

Figure 3. Transmission electron microscope (TEM) images of (**a**) $BiOBr_{0.75}I_{0.25}$ and (**b**) $BiOBr_{0.25}I_{0.75}$.

2.2. Optical Absorption and Photocatalytic Properties

The optical properties of $BiOBr_xI_{1-x}$ solid solutions were investigated by UV-vis DRS spectra and the results are illustrated in Figure 4a. It can be obviously seen that for the end-member samples, the absorption threshold of BiOBr is about 438.5 nm, whereas this value of BiOI is near 674.1 nm, suggesting that both of them can be excited by visible light. As expected, the absorption thresholds of the other three $BiOBr_xI_{1-x}$ solid solutions are all located between those of BiOBr and BiOI, and regularly increase with I content increasing. The optical band gap (E_g) of a semiconductor photocatalyst can be determined by extrapolation of the linear portion of $[F(R)\cdot h\nu]^{0.5}$ curve versus photon energy $h\nu$ to $[F(R)\cdot h\nu]^{0.5} = 0$ [45]. Based on the above UV-vis DRS results, E_g values of $BiOBr_xI_{1-x}$ solid solutions were obtained as shown in Figure 4b and Table 1. Interestingly, as I content increases, E_g values of $BiOBr_xI_{1-x}$ samples gradually decrease. This also indicates that the as-prepared products are a group of $BiOBr_xI_{1-x}$ solid solutions. The regular changes in optical absorption threshold and E_g value strongly state that the substitution of smaller Br ions by larger I ions can modify the optical absorption property and band structure of $BiOBr_xI_{1-x}$ solid solutions. It has been verified that, for BiOX semiconductors, the CBM is dominated by Bi 6p orbitals and the VBM mainly originates from O 2p and X *n*p orbitals (n = 3, 4 and 5 for X = Cl, Br and I, respectively) [24,30]. Therefore, as I content increases, the contribution of I 5p orbitals dramatically increases and, correspondingly, the band gap is narrowed down.

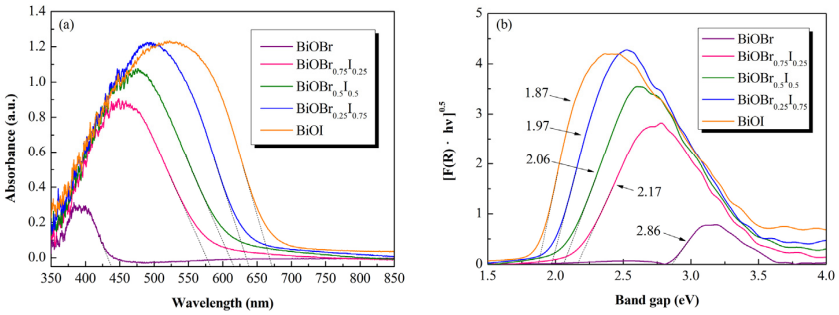

Figure 4. (**a**) UV-vis diffuse reflectance spectra (UV-vis DRS) spectra of $BiOBr_xI_{1-x}$ solid solutions; (**b**) relationships between $[F(R)\cdot h\nu]^{0.5}$ and band gap.

The photocatalytic properties of $BiOBr_xI_{1-x}$ solid solutions were investigated by evaluating the degradation of RhB under simulated sunlight irradiation. Figure 5a illustrates the photocatalytic degradation of RhB over $BiOBr_xI_{1-x}$ solid solutions with 60 min adsorption in dark followed by 180 min photocatalysis under simulated sunlight irradiation. It is well known that the adsorption plays an essential role in the heterogeneous photocatalytic process [45]. The results clearly reveal that the adsorbed amounts of RhB onto $BiOBr_xI_{1-x}$ samples with different x values are almost alike at the adsorption/desorption equilibrium, consequently, the influence of adsorption capacity on photocatalytic evaluation can be neglected. It can also be found that $BiOBr_xI_{1-x}$ solid solutions with x = 0.25, 0.5, and 0.75 exhibit higher photocatalytic activity than the end-member BiOBr and BiOI. Only 31.6% and 77.7% of RhB can be degraded over BiOI and BiOBr, respectively, within 240 min reaction time; nevertheless, almost all the RhB can be degraded over $BiOBr_{0.75}I_{0.25}$ and $BiOBr_{0.5}I_{0.5}$ within 210 and 240 min reaction time, respectively. The BET specific surface areas of BiOBr, $BiOBr_{0.75}I_{0.25}$, $BiOBr_{0.5}I_{0.5}$, $BiOBr_{0.25}I_{0.75}$, and BiOI were determined to be 7.14, 6.71, 7.30, 6.19, and 6.28 m^2/g, respectively. Since there is no obvious difference in their surface areas, the enhanced photocatalytic activities of $BiOBr_{0.75}I_{0.25}$, $BiOBr_{0.5}I_{0.5}$, and $BiOBr_{0.25}I_{0.75}$ are not essentially related to the surface area. It is very obvious that, among them, $BiOBr_{0.75}I_{0.25}$ exhibits the best photocatalytic activity. This conclusion is similar to Zhang's report [39]. Furthermore, Figure 5b indicates that the RhB photodegradation processes followed a pseudo-first-order kinetic equation:

$$\ln(C/C_0) = kt \quad (1)$$

where C_0 is the initial RhB concentration, C is the residual RhB concentration at time t, and the slope k is the apparent reaction rate constant. The calculated apparent reaction rate constants are listed is Table 1. The k value of $BiOBr_{0.75}I_{0.25}$ is approximately 15.1 times higher than that of BiOI and approximately 3.4 times higher than that of BiOBr, indicating an enhanced photocatalytic activity of $BiOBr_xI_{1-x}$ solid solutions with x = 0.75.

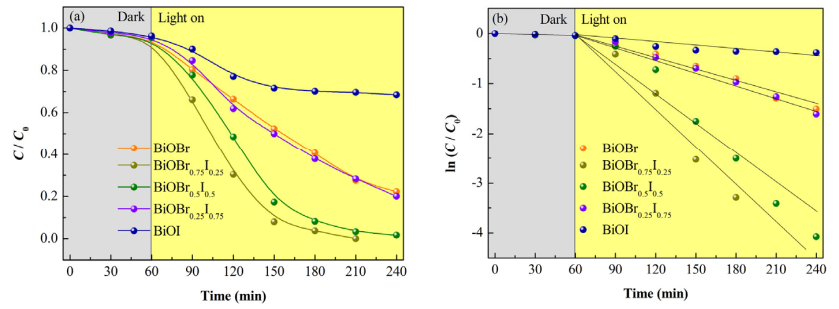

Figure 5. (**a**) Photocatalytic degradation of RhB over $BiOBr_xI_{1-x}$ solid solutions under simulated sunlight irradiation; (**b**) pseudo-first-order kinetic curves of RhB photodegradation processes.

The chemical oxygen demand (COD) of RhB solution after different photodegradation periods over $BiOBr_{0.75}I_{0.25}$ was detected and the results are displayed in Figure 6a. It can be seen that more than 90% COD in RhB solution can be eliminated after 210 min reaction, which implies that most RhB molecules can be decomposed into H_2O and CO_2 in this photocatalytic system. Moreover, the UV-vis absorption peaks of RhB solution after different photodegradation periods gradually weaken (Figure 6b), also indicating an almost complete decomposition of RhB molecules. Thereby, it can be inferred that almost all the RhB molecules are decomposed into H_2O, CO_2, and small molecule organics. Photocatalytic stability is another important parameter to evaluate a photocatalyst. The recyclability of $BiOBr_xI_{1-x}$ solid solution photocatalysts was evaluated, also using $BiOBr_{0.75}I_{0.25}$ as the representative sample. Figure 7a reveals that, even after 5 runs, $BiOBr_{0.75}I_{0.25}$ photocatalyst still has high photocatalytic activity. As shown in Figure 7b, the XRD result indicates that $BiOBr_{0.75}I_{0.25}$ sample after being circularly used 5 times maintains the crystal structure of bismuth oxyhalide without any destruction. These suggest that $BiOBr_xI_{1-x}$ solid solutions not only have excellent photocatalytic stability but also possess good structural stability.

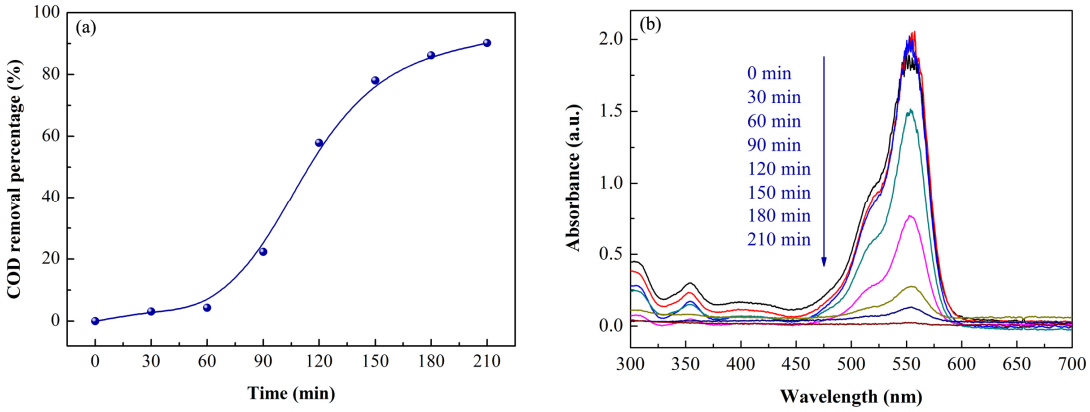

Figure 6. (**a**) Chemical oxygen demand (COD) removal percentage and (**b**) UV-vis absorption spectra of RhB solution after different photodegradation periods over $BiOBr_{0.75}I_{0.25}$.

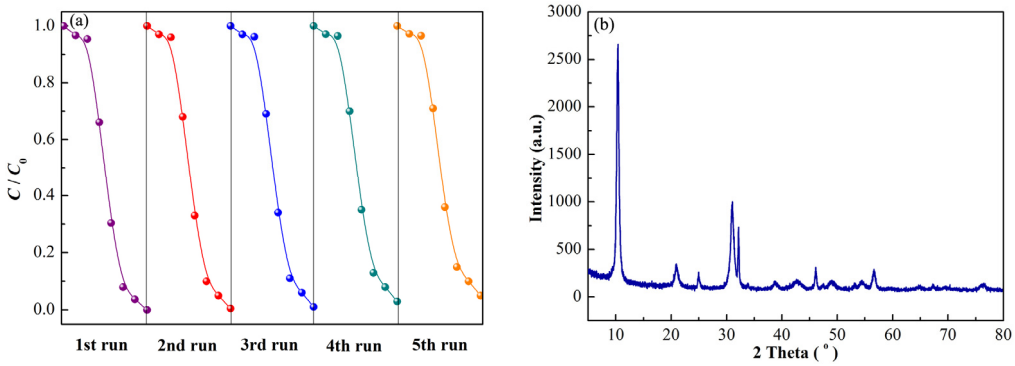

Figure 7. (**a**) Cycling experiments on RhB photodegradation over $BiOBr_{0.75}I_{0.25}$; (**b**) XRD pattern of $BiOBr_{0.75}I_{0.25}$ after being circularly used 5 times.

2.3. Structure-Dependent Photocatalytic Performance

In a typical photocatalytic process, three key steps are involved in the charge kinetics. Firstly, electron-hole pairs are generated under photoexcitation; then, the photogenerated charges transfer to the catalyst surface; finally, these charges participate in the redox reactions on the catalyst surface. Thus, in order to construct highly efficient photocatalysts, the aim of structure engineering is mainly to improve the efficiency of each step in the charge kinetics. To this end, the structure engineering

specifically includes surface engineering, interface engineering, and energy band engineering [46]. Since the facets constitute the surface and interface of a photocatalyst, they have strong influence on the structure and property of surface and interface, and should be rationally selected. The facets exposed on a photocatalyst surface may affect the photocatalytic performance through various working mechanisms [47]. The photocatalytic performance of $BiOBr_xI_{1-x}$ solid solutions strongly depends on their crystal structures as well.

The typical layered structures of BiOX along the *b*- and *c*-axes are illustrated in Figure 8a,b, respectively. In this structure, all the atoms of the asymmetric unit lie on special positions, 4 mm or $\bar{4}$ m^2. One bismuth atom is coordinated with four oxygen and four halogen atoms to form an asymmetric decahedral geometry, which is linked with each other by sharing the O-X edge along the *a*- and *b*-axes. $[Bi_2O_2]^{2+}$ layers are interleaved by double layers of halogen ions. The inhomogeneity of charge distribution between $[Bi_2O_2]^{2+}$ and halogen layers in this asymmetric structure can form the IEF along the *c*-axis (Figure 8c) [24]. IEF can efficiently separate the photogenerated electrons and holes, drive them to $[Bi_2O_2]$ and [X] layers respectively, and accommodate them within $[Bi_2O_2]$ and [X] layers to prevent their recombination [48]. Moreover, the interlayer van der Waals interactions and intralayer covalent bonding can facilitate the preparation of BiOX nanoplates with highly exposed {001} facets [30]. It has been verified that the IEF magnitude of BiOX nanoplates is proportional to their exposure amounts of {001} facets [41]. Hence, the higher photocatalytic activity of {001} facet-dominant BiOX nanoplates profits from stronger IEF that can promote electron-hole transfer and inhibit their recombination [24].

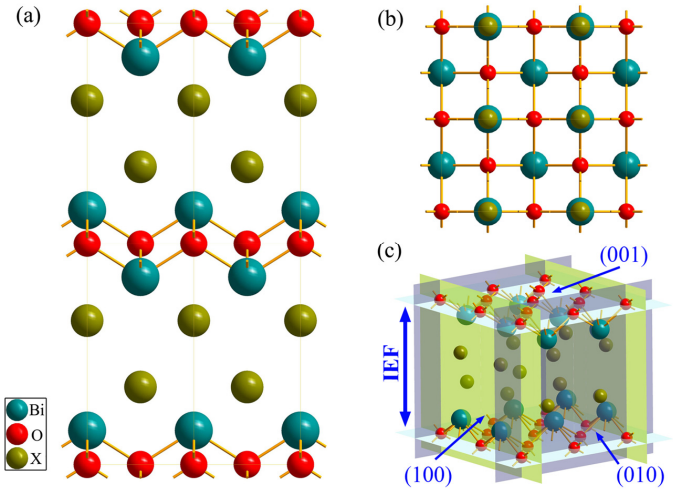

Figure 8. (**a**,**b**) crystal structure projection of BiOX along *b*- and *c*-axis, respectively; (**c**) diagram of internal electric fields (IEF) perpendicular to (001) crystal plane.

By carefully examining the XRD patterns in this study, we found that $BiOBr_xI_{1-x}$ solid solutions with different *x* values had different diffraction intensities of (001) peak. In regard to BiOX crystals, the exposure amount of {001} facets should be in direct proportion to the relative intensity of (001) peak [43]. Analogous to the method reported by Zhang's group [49], the intensity ratio of the (001) and (102) peaks were employed to approximately estimate the exposure amount of {001} facets in each sample. Figure 9a obviously indicates that the {001} facets exposure amount for $BiOBr_xI_{1-x}$ samples is in the following order: BiOI > $BiOBr_{0.5}I_{0.5}$ > $BiOBr_{0.25}I_{0.75}$ > $BiOBr_{0.75}I_{0.25}$ > BiOBr. Because the IEF magnitude is in direct proportion to the exposure amounts of {001} facets, it can be deemed that the IEF magnitude of $BiOBr_xI_{1-x}$ samples is in the same sequence. Hereby, it is plausible that BiOI should have the best photocatalytic activity among these samples. However, the experimental data generated in this study does not follow this trend, as shown in Figure 5a. The possible explanation for this phenomenon might be ascribed to two aspects. On one hand, according to Bragg's formula, $\lambda = 2d\sin\theta$, the regular

shift of (001) peak to smaller diffraction angle indicates an increase in the interlayer spacing of (001) crystal plane, as I content in $BiOBr_xI_{1-x}$ solid solutions increases. Figure 9b displays the gradual increase in interlayer spacing of (001) crystal plane, d_{001}. This result provides strong evidence to certify the formation of intercalated layered products [50]. Importantly, the increase in d_{001} would make the distance longer for charge transport driven by IEF, reducing the effective separation of photogenerated electron-hole pairs and thereby decreasing the photocatalytic activity. So, the largest (001) interlayer spacing of BiOI negatively affects its photocatalytic performance.

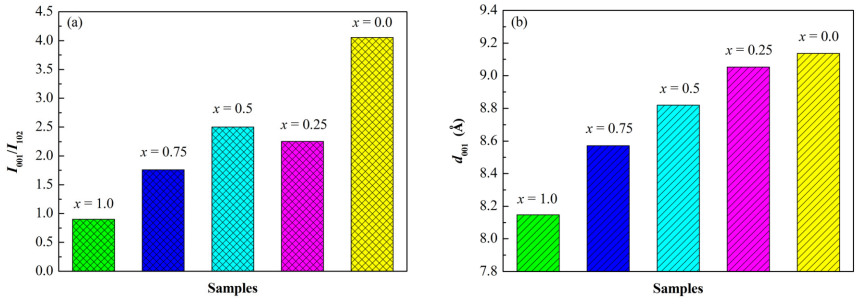

Figure 9. (**a**) I_{001}/I_{102} and (**b**) d_{001} of $BiOBr_xI_{1-x}$ solid solutions with different x values.

On the other hand, the different energy levels of hybrid orbitals can be formed due to the different molar ratios of Br and I in $BiOBr_xI_{1-x}$ solid solutions, which means that their band structures can be modulated by changing the molar ratio of Br and I. In order to further know the relationship between band structure and photocatalytic activity of $BiOBr_xI_{1-x}$ samples, the energy-level positions of VBM and CBM were calculated by Equations (2) and (3) [51–53]:

$$E_{CB} = \chi + E^{\circ} - 0.5E_g \quad (2)$$

$$E_{VB} = \chi + E^{\circ} + 0.5E_g \quad (3)$$

where, E_{CB} and E_{VB} are the energy levels of CBM and VBM, respectively; χ is the absolute electronegativity of a semiconductor, namely the geometric mean value of the absolute electronegativity of each atom in the semiconductor; E° is the scale factor relating the reference electrode redox level to the absolute vacuum scale, determined to be −4.5 eV for normal hydrogen electrode; and E_g is the band-gap energy of the semiconductor. The calculated results are listed in Table 1. It can be obviously seen in Figure 10 that CBM potentials of all the samples are positive, implying that the photogenerated electrons in conduction band cannot react with O_2 to form O_2^- radicals (O_2/O_2^- = −0.28 V); nevertheless, VBM potentials of these samples are all more positive than +1.99 V, indicating that the photogenerated holes in the valence band are anodic enough to oxidize H_2O or OH^- into OH radicals (OH/OH^- = +1.99 V) [54]. Meanwhile, as x value increases, the potential of VBM gradually increases. The deeper VBM position can result in higher oxidation power of the photogenerated holes [55], which can directly oxidize the organic molecules or react with adsorbed H_2O and surface OH^- to form highly reactive OH radicals. Hence, BiOI exhibits the worst photocatalytic oxidation power among $BiOBr_xI_{1-x}$ solid solutions, attributed to its lowest VBM potential.

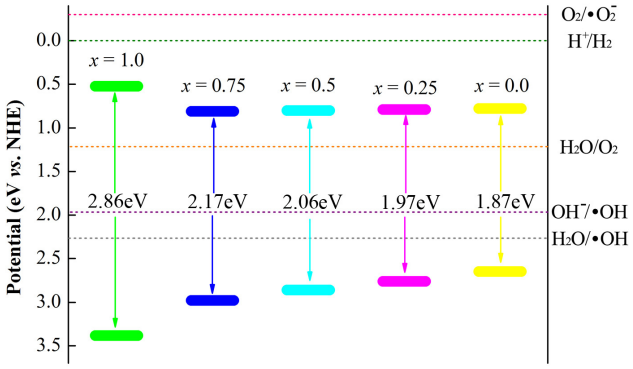

Figure 10. Schematic illustration of the band structures of $BiOBr_xI_{1-x}$ solid solutions.

According to above discussions, it can be concluded that the photocatalytic performance of $BiOBr_xI_{1-x}$ solid solutions is closely dependent on their structures, including exposure amount of {001} facets, interlayer spacing of (001) plane, and electronic band structure. When $BiOBr_xI_{1-x}$ semiconductor is irradiated by simulated sun light, the photogenerated electrons and holes can be produced, which are the main initiators to form the highly oxidative species. Nevertheless, they are easy to recombine together, consequently reducing the photocatalytic activity. As shown in Figure 11, driven by the IEF, photogenerated electrons and holes can be separated and transported to $[Bi_2O_2]$ and [X] layers, respectively. Since the IEF is perpendicular to (001) crystal plane, more exposure amount of {001} facets can lead to a larger IEF, which can more efficiently induce the separation and transport of photogenerated charges. However, larger interlayer spacing of (001) plane is not conducive to the separation and transport of photogenerated charges because of the longer distance along the IEF. Moreover, the deeper energy-level position of VB can make the photogenerated holes have more powerful oxidation ability. Therefore, the synergistic effect of these three structural factors determines the photocatalytic performance of $BiOBr_xI_{1-x}$ solid solutions.

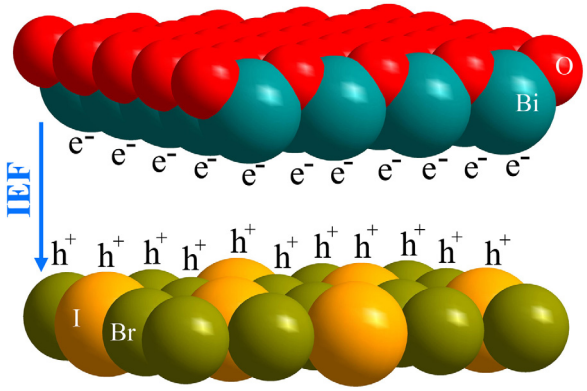

Figure 11. Schematic illustration of the separation and transport of photogenerated electron-hole pairs driven by IEF.

3. Materials and Methods

3.1. Preparation of $BiOBr_xI_{1-x}$ Solid Solutions

All the chemical reagents used in this work were of analytical grade and were without further purification. An alcoholysis method with facile operation and low cost was employed for the preparation of $BiOBr_xI_{1-x}$ nanoplate solid solutions at room temperature and atmospheric pressure. Bismuth nitrate pentahydrate ($Bi(NO_3)_3 \cdot 5H_2O$, Tianjin Ruijinte Chemical Reagent Co., Ltd., Tianjin, China), potassium bromide (KBr, Tianjin Zhiyuan Chemical Reagent Co., Ltd., Tianjin, China), and

potassium iodide (KI, Tianjin Tianda Chemical Reagent Co., Ltd., Tianjin, China) were used as Bi, Br, and I sources, respectively. In a typical procedure, certain amounts of $Bi(NO_3)_3 \cdot 5H_2O$ were put into a 200 mL beaker and some volume of absolute ethyl alcohol (Tianjin Tianli Chemical Reagent Co., Ltd., Tianjin, China) was subsequently injected. Then, the resulting suspensions underwent an alcoholysis process under ultrasonic irradiation until $Bi(NO_3)_3 \cdot 5H_2O$ was completely dissolved in absolute ethyl alcohol. At the same time, according to the stoichiometric value x (0, 0.25, 0.5, 0.75, and 1.0) in $BiOBr_xI_{1-x}$ solid solutions, some amount of KBr and KI was weighed and dissolved in a small quantity of deionized water. Afterwards, this solution was added to the above obtained alcoholysate and the mixture was mechanically stirred for 6 h at room temperature. Thereafter, the final suspension was centrifuged and the resulting precipitate was washed by absolute ethyl alcohol and deionized water alternately until the filtrate reached neutral. After being dried at 80 °C for six hours and ground, the powder of $BiOBr_xI_{1-x}$ nanoplate solid solutions was obtained for later use, which was labeled as BiOBr, $BiOBr_{0.75}I_{0.25}$, $BiOBr_{0.5}I_{0.5}$, $BiOBr_{0.25}I_{0.75}$, and BiOI with x = 1.0, 0.75, 0.5, 0.25, and 0.0, respectively.

3.2. Characterization Techniques

XRD was employed for the identification of samples' crystal phase by a PANalytical X'Pert X-ray diffractometer (PANalytical Company Inc., Almelo, The Netherlands) using Cu-K_α radiation (λ = 0.15418 nm) over the range of 10–80° with a voltage of 40 kV and an electric current of 40 mA. The microscopic morphologies of $BiOBr_xI_{1-x}$ nanoplate solid solutions were observed by FESEM and TEM, which were implemented on FEISirion200 scanning electron microscope equipped with EDS (FEI Company Inc., Eindhoven, The Netherlands) and JEOL JEM-2100 transmission electron microscope (JEOL Ltd., Tokyo, Japan), respectively. UV-vis DRS spectra were recorded on an USB4000 UV-vis spectrometer (Ocean Optics Inc., Dunedin, FL, USA) equipped with an integral sphere using a standard template provided by South Africa Optics as the reference. The BET specific surface area of samples was obtained from nitrogen adsorption-desorption data and measured using a Sibata SA-1100 surface area analyzer (Sibata Ltd., Kyoto, Japan) at liquid nitrogen temperature. The atomic configuration of BiOX was realized by Diamond program version 3.1 (Crystal and Molecular Structure Visualization, Crystal Impact, Bonn, Germany). The cell parameters a and c of $BiOBr_xI_{1-x}$ solid solutions were obtained by UnitCell software (a non-linear least squares cell refinement program with regression diagnostics, designed by Tim Holland & Simon Redfern), according to a least-squares calculation from 2θ values in XRD patterns. The interlayer spacing of (001) crystal plane was calculated by the well-known Bragg's Law, $\lambda = 2d\sin\theta$, based on 2θ value corresponding to (001) crystal plane.

3.3. Photocatalytic Evaluation

A 300 W Xe lamp with a power of 100 mW/cm^2 was used as the simulated sunlight in the whole photocatalytic process. One hundred milligrams of $BiOBr_xI_{1-x}$ photocatalyst was added to 100 mL RhB solution with the initial concentration (C_0) of 20 mg/L. Before irradiation by simulated solar light, the suspension was stirred in the dark for 60 min to reach the adsorption and desorption equilibrium. After that, the Xe lamp was turned on and photocatalytic reaction started under continuous stirring. At regular time intervals (30 min) of the photocatalytic reaction, 5 mL of the suspension solution was taken out and centrifuged for 10 min to obtain the supernatant. The residual RhB concentration (C) in the supernatant was detected by a 722-type UV-vis spectrophotometer at RhB maximum absorption wavelength of 553 nm. The detection of chemical oxygen demand (COD) in solution was implemented by fast-digestion spectrophotometric method (Chinese Standard HJ/T 399-2007). The residual dye solution after different reaction periods was also analyzed by UV-vis absorption spectra (USB4000 UV-vis spectrometer, Ocean Optics).

4. Conclusions

A group of $BiOBr_xI_{1-x}$ solid solutions was successfully obtained at room temperature and atmospheric pressure. These samples exhibited 2D plate-like structure with high {001} facets exposure.

As I content increased, E_g values of $BiOBr_xI_{1-x}$ samples decreased, which strongly indicated that the substitution of smaller Br ions by larger I ions could modify their optical absorption properties. $BiOBr_xI_{1-x}$ solid solutions with x = 0.75 exhibited the highest photocatalytic activity. The intensity ratio of the (001) and (102) peaks suggested that {001} facets exposure amount for $BiOBr_xI_{1-x}$ samples was in the following order: BiOI > $BiOBr_{0.5}I_{0.5}$ > $BiOBr_{0.25}I_{0.75}$ > $BiOBr_{0.75}I_{0.25}$ > BiOBr. The regular shift of (001) peak to smaller diffraction angle indicated an increase in the interlayer spacing of (001) crystal plane with I content increasing. This might negatively affect their photocatalytic performances. As I content increased, the potentials of VBM for $BiOBr_xI_{1-x}$ solid solutions gradually decreased. The synergistic effect of these three structural factors determined the photocatalytic performance of $BiOBr_xI_{1-x}$ solid solutions.

Acknowledgments: This work was financially supported by the Natural Science Foundation of Heilongjiang Province, China (No. E2015065).

Author Contributions: Huan-Yan Xu conceived and designed the experiments; Xu Han and Qu Tan performed the experiments; Huan-Yan Xu, Xu Han, Qu Tan, Xiu-Lan He, and Shu-Yan Qi analyzed the data; Huan-Yan Xu contributed reagents/materials/analysis tools; Huan-Yan Xu and Qu Tan wrote the paper; Huan-Yan Xu constructed the crystal model.

Conflicts of Interest: The authors declare no conflict of interest.

References

1. Piccirillo, C.; Castro, P.M.L. Calcium hydroxyapatite–based photocatalysts for environment remediation: Characteristics, performances and future perspectives. *J. Environ. Manag.* **2017**, *193*, 79–91. [CrossRef] [PubMed]
2. Ren, H.J.; Koshy, P.; Chen, W.F.; Qi, S.H.; Sorrell, C.C. Photocatalytic materials and technologies for air purification. *J. Hazard. Mater.* **2017**, *325*, 340–366. [CrossRef] [PubMed]
3. Yadav, H.M.; Kim, J.S.; Pawar, S.H. Developments in photocatalytic antibacterial activity of nano TiO_2: A review. *Korean J. Chem. Eng.* **2016**, *33*, 1989–1998. [CrossRef]
4. Colon, G. Towards the hydrogen production by photocatalysis. *Appl. Catal. A Gen.* **2016**, *518*, 48–59. [CrossRef]
5. Ouyang, S.X.; Tong, H.; Umezawa, N.; Cao, J.Y.; Li, P.; Bi, Y.P.; Zhang, Y.J.; Ye, J.H. Surface-alkalinization-induced enhancement of photocatalytic H_2 evolution over $SrTiO_3$—Based photocatalysts. *J. Am. Chem. Soc.* **2012**, *134*, 1974–1977. [CrossRef] [PubMed]
6. Molinari, R.; Lavorato, C.; Argurio, P. Recent progress of photocatalytic membrane reactors in water treatment and in synthesis of organic compounds: A review. *Catal. Today* **2017**, *281*, 144–164. [CrossRef]
7. Zhou, P.; Yu, J.G.; Jaroniec, M. All-solid-state Z-scheme photocatalytic systems. *Adv. Mater.* **2014**, *26*, 4920–4935. [CrossRef] [PubMed]
8. Prashant, V.K. TiO_2 nanostructures: Recent physical chemistry advances. *J. Phys. Chem. C* **2012**, *116*, 11849–11851. [CrossRef]
9. Kim, T.W.; Hur, S.G.; Hwang, S.J.; Park, H.W.; Choi, W.Y.; Choy, J.H. Heterostructured visible–light–active photocatalyst of chromia-nanoparticle-layered titanate. *Adv. Funct. Mater.* **2007**, *17*, 307–314. [CrossRef]
10. Chen, X.B.; Liu, L.; Yu, P.Y.; Mao, S.S. Increasing solar absorption for photocatalysis with black hydrogenated titanium dioxide nanocrystals. *Science* **2011**, *331*, 746–750. [CrossRef] [PubMed]
11. Gomis-Berenguer, A.; Velasco, L.F.; Velo-Gala, I.; Ania, C.O. Photochemistry of nanoporous carbons: Perspectives in energy conversion and environmental remediation. *J. Colloid Interface Sci.* **2017**, *490*, 879–901. [CrossRef] [PubMed]
12. Reddy, D.A.; Ma, R.; Choi, M.Y.; Kim, T.K. Reduced graphene oxide wrapped ZnS—Ag_2S ternary composites synthesized via hydrothermal method: Applications in photocatalyst degradation of organic pollutants. *Appl. Surf. Sci.* **2015**, *324*, 725–735. [CrossRef]
13. Reddy, D.A.; Choi, J.; Lee, S.; Ma, R.; Kim, T.K. Self-assembled macro porous ZnS-graphene aerogels for photocatalytic degradation of contaminants in water. *RSC Adv.* **2015**, *5*, 18342–18351. [CrossRef]
14. Reddy, D.A.; Lee, S.; Choi, J.; Park, S.; Ma, R.; Yang, H.; Kim, T.K. Green synthesis of AgI-reduced graphene oxide nanocomposites: Toward enhanced visible–light photocatalytic activity for organic dye removal. *Appl. Surf. Sci.* **2015**, *341*, 175–184. [CrossRef]

15. Reddy, D.A.; Choi, J.; Lee, S.; Ma, R.; Kim, T.K. Green synthesis of AgI nanoparticle-functionalized reduced graphene oxide aerogels with enhanced catalytic performance and facile recycling. *RSC Adv.* **2015**, *5*, 67394–67404. [CrossRef]
16. Choi, J.; Reddy, D.A.; Kim, T.K. Enhanced photocatalytic activity and anti-photocorrosion of AgI nanostructures by coupling with graphene-analogue boron nitride nanosheets. *Ceram. Int.* **2015**, *41*, 13793–13803. [CrossRef]
17. Islam, M.J.; Reddy, D.A.; Han, N.S.; Choi, J.; Song, J.K.; Kim, T.K. An oxygen-vacancy rich 3D novel hierarchical MoS_2/BiOI/AgI ternary nanocomposite: Enhanced photocatalytic activity through photogenerated electron shuttling in a Z-scheme manner. *Phys. Chem. Chem. Phys.* **2016**, *18*, 24984–24993. [CrossRef] [PubMed]
18. Choi, J.; Reddy, D.A.; Islam, M.J.; Ma, R.; Kim, T.K. Self-assembly of CeO_2 nanostructures/reduced graphene oxide composite aerogels for efficient photocatalytic degradation of organic pollutants in water. *J. Alloys Compd.* **2016**, *688*, 527–536. [CrossRef]
19. Reddy, D.A.; Choi, J.; Lee, S.; Kim, T.K. Controlled synthesis of heterostructured Ag@AgI/ZnS microspheres with enhanced photocatalytic activity and selective separation of methylene blue from mixture dyes. *J. Taiwan Inst. Chem. Eng.* **2016**, *66*, 200–209. [CrossRef]
20. Lee, S.; Reddy, D.A.; Kim, T.K. Well-wrapped reduced graphene oxide nanosheets on $Nb_3O_7(OH)$ nanostructures as good electron collectors and transporters for efficient photocatalytic degradation of rhodamine B and phenol. *RSC Adv.* **2016**, *6*, 37180–37188. [CrossRef]
21. Bhachu, D.S.; Moniz, S.J.A.; Sathasivam, S.; Scanlon, D.O.; Walsh, A.; Bawaked, S.M.; Mokhtar, M.; Obaid, A.Y.; Parkin, I.P.; Tang, J.W.; et al. Bismuth oxyhalides: Synthesis, structure and photoelectrochemical activity. *Chem. Sci.* **2016**, *7*, 4832–4841. [CrossRef]
22. Keramidas, K.G.; Voutsas, G.P.; Rentzeperis, P.I. The crystal structure of BiOCl. *Z. Kristallogr.* **1993**, *205*, 35–40.
23. Bannister, F.A.; Hey, M.H. The crystal-structure of the bismuth oxyhalides. *Mineral. Mag.* **1935**, *24*, 49–58. [CrossRef]
24. Li, J.; Yu, Y.; Zhang, L.Z. Bismuth oxyhalide nanomaterials: Layered structures meet photocatalysis. *Nanoscale* **2014**, *6*, 8473–8488. [CrossRef] [PubMed]
25. Xu, Z.F.; Hao, W.C.; Zhang, Q.F.; Fu, Z.H.; Feng, H.F.; Du, Y.; Dou, S.X. Indirect-direct band transformation of few-layer BiOCl under biaxial strain. *J. Phys. Chem. C* **2016**, *120*, 8589–8594. [CrossRef]
26. Qin, Q.; Guo, Y.N.; Zhou, D.D.; Yang, Y.X.; Guo, Y.H. Facile growth and composition-dependent photocatalytic activity of flowerlike $BiOCl_{1-x}Br_x$ hierarchical microspheres. *Appl. Surf. Sci.* **2016**, *390*, 765–777. [CrossRef]
27. Liu, Y.Y.; Son, W.J.; Lu, J.B.; Huang, B.B.; Dai, Y.; Whangbo, M.H. Composition dependence of the photocatalytic activities of $BiOCl_{1-x}Br_x$ solid solutions under visible light. *Chem. Eur. J.* **2011**, *17*, 9342–9349. [CrossRef] [PubMed]
28. Gnayem, H.; Sasson, Y. Hierarchical nanostructured 3D flowerlike $BiOCl_xBr_{1-x}$ semiconductors with exceptional visible light photocatalytic activity. *ACS Catal.* **2013**, *3*, 186–191. [CrossRef]
29. Mao, X.M.; Fan, C.M. Effect of light response on the photocatalytic activity of $BiOCl_xBr_{1-x}$ in the removal of Rhodamine B from water. *Int. J. Miner. Metall. Mater.* **2013**, *20*, 1089–1095. [CrossRef]
30. Zhang, X.; Wang, L.W.; Wang, C.Y.; Wang, W.K.; Chen, Y.L.; Huang, Y.X.; Li, W.W.; Feng, Y.J.; Yu, H.Q. Synthesis of $BiOCl_xBr_{1-x}$ nanoplate solid solutions as a robust photocatalyst with tunable band structure. *Chem. Eur. J.* **2015**, *21*, 11872–11877. [CrossRef] [PubMed]
31. Du, D.D.; Li, W.J.; Chen, S.S.; Yan, T.J.; You, J.M.; Kong, D.S. Synergistic degradation of rhodamine B on $BiOCl_xBr_{1-x}$ sheets by combined photosensitization and photocatalysis under visible light irradiation. *New J. Chem.* **2015**, *39*, 3129–3136. [CrossRef]
32. Li, T.B.; Chen, G.; Zhou, C.; Shen, Z.Y.; Jin, R.C.; Sun, J.X. New photocatalyst BiOCl/BiOI composites with highly enhanced visible light photocatalytic performances. *Dalton Trans.* **2011**, *40*, 6751–6758. [CrossRef] [PubMed]
33. Xiao, X.; Hao, R.; Liang, M.; Zuo, X.; Nan, J.; Li, L.; Zhang, W. One-pot solvothermal synthesis of three-dimensional (3D) BiOI/BiOCl composites with enhanced visible-light photocatalytic activities for the degradation of bisphenol-A. *J. Hazard. Mater.* **2012**, *233–234*, 122–130. [CrossRef] [PubMed]

34. Sun, L.M.; Xiang, L.; Zhao, X.; Jia, C.J.; Yang, J.; Jin, Z.; Cheng, X.F.; Fan, W.L. Enhanced visible-light photocatalytic activity of BiOI/BiOCl heterojunctions: Key role of crystal facet combination. *ACS Catal.* **2015**, *5*, 3540–3551. [CrossRef]
35. Yang, C.Y.; Li, F.; Zhang, M.; Li, T.H.; Cao, W. Preparation and first-principles study for electronic structures of BiOI/BiOCl composites with highly improved photocatalytic and adsorption performances. *J. Mol. Catal. A Chem.* **2016**, *423*, 1–11. [CrossRef]
36. Jia, Z.F.; Wang, F.M.; Xin, F.; Zhang, B.Q. Simple solvothermal routes to synthesize 3D $BiOBr_xI_{1-x}$ microspheres and their visible-light-induced photocatalytic properties. *Ind. Eng. Chem. Res.* **2011**, *50*, 6688–6694. [CrossRef]
37. Lin, L.; Huang, M.H.; Long, L.P.; Sun, Z.; Zheng, W.; Chen, D.H. Fabrication of a three-dimensional BiOBr/BiOI photocatalyst with enhanced visible light photocatalytic performance. *Ceram. Int.* **2014**, *40*, 11493–11501. [CrossRef]
38. Zheng, C.R.; Cao, C.B.; Alia, Z. In situ formed Bi/$BiOBr_xI_{1-x}$ heterojunction of hierarchical microspheres for efficient visible-light photocatalytic activity. *Phys. Chem. Chem. Phys.* **2015**, *17*, 13347–13354. [CrossRef] [PubMed]
39. Zhang, X.; Wang, C.Y.; Wang, L.W.; Huang, G.X.; Wang, W.K.; Yu, H.Q. Fabrication of $BiOBr_xI_{1-x}$ photocatalysts with tunable visible light catalytic activity by modulating band structures. *Sci. Rep.* **2016**, *6*, 22800. [CrossRef] [PubMed]
40. Chen, H.B.; Yu, X.; Zhu, Y.; Fu, X.H.; Zhang, Y.M. Controlled synthesis of {001} facets-dominated dye-sensitized BiOCl with high photocatalytic efficiency under visible-light irradiation. *J. Nanopart. Res.* **2016**, *18*, 225. [CrossRef]
41. Li, J.; Zhang, L.Z.; Li, Y.J.; Yu, Y. Synthesis and internal electric field dependent photoreactivity of Bi_3O_4Cl single-crystalline nanosheets with high {001} facet exposure percentages. *Nanoscale* **2014**, *6*, 167–171. [CrossRef] [PubMed]
42. Lei, Y.Q.; Wang, G.H.; Song, S.Y.; Fan, W.Q.; Zhang, H.J. Synthesis, characterization and assembly of BiOCl nanostructure and their photocatalytic properties. *CrystEngComm* **2009**, *11*, 1857–1862. [CrossRef]
43. Li, H.; Shi, J.G.; Zhao, K.; Zhang, L.Z. Sustainable molecular oxygen activation with oxygen vacancies on the {001} facets of BiOCl nanosheets under solar light. *Nanoscale* **2014**, *6*, 14168–14173. [CrossRef] [PubMed]
44. Feng, H.F.; Xu, Z.F.; Wang, L.; Yu, Y.X.; Mitchell, D.; Cui, D.D.; Xu, X.; Shi, J.; Sannomiya, T.; Du, Y.; et al. Modulation of photocatalytic properties by strain in 2D BiOBr nanosheets. *ACS Appl. Mater. Interfaces* **2015**, *7*, 27592–27596. [CrossRef] [PubMed]
45. Xu, H.Y.; Wu, L.C.; Jin, L.G.; Wu, K.J. Combination mechanism and enhanced visible-light photocatalytic activity and stability of CdS/g-C_3N_4 heterojunctions. *J. Mater. Sci. Technol.* **2017**, *33*, 30–38. [CrossRef]
46. Bai, S.; Jiang, W.Y.; Li, Z.Q.; Xiong, Y.J. Surface and interface engineering in photocatalysis. *ChemNanoMat* **2015**, *1*, 223–239. [CrossRef]
47. Bai, S.; Wang, L.L.; Li, Z.Q.; Xiong, Y.J. Facet-engineered surface and interface design of photocatalytic materials. *Adv. Sci.* **2017**, *4*, 1600216. [CrossRef] [PubMed]
48. Li, J.; Li, H.; Zhan, G.M.; Zhang, L.Z. Solar water splitting and nitrogen fixation with layered bismuth oxyhalides. *Acc. Chem. Res.* **2017**, *50*, 112–121. [CrossRef] [PubMed]
49. Jiang, J.; Zhao, K.; Xiao, X.Y.; Zhang, L.Z. Synthesis and facet-dependent photoreactivity of BiOCl single-crystalline nanosheets. *J. Am. Chem. Soc.* **2012**, *134*, 4473–4476. [CrossRef] [PubMed]
50. Zhang, Y.Y.; Sun, X.G.; Yang, G.Z.; Zhu, Y.H.; Si, H.Y.; Zhang, J.M.; Li, Y.T. Preparation and characterization of bifunctional $BiOCl_xI_y$ solid solutions with excellent adsorption and photocatalytic abilities for removal of organic dyes. *Mater. Sci. Semicond. Process.* **2016**, *41*, 193–199. [CrossRef]
51. Zhang, W.D.; Zhang, Q.; Dong, F. Visible-light photocatalytic removal of NO in air over BiOX (X = Cl, Br, I) single-crystal nanoplates prepared at room temperature. *Ind. Eng. Chem. Res.* **2013**, *52*, 6740–6746. [CrossRef]
52. Shang, J.; Hao, W.C.; Lv, X.J.; Wang, T.M.; Wang, X.L.; Du, Y.; Dou, S.X.; Xie, T.F.; Wang, D.J.; Wang, J.O. Bismuth oxybromide with reasonable photocatalytic reduction activity under visible light. *ACS Catal.* **2014**, *4*, 954–961. [CrossRef]
53. Wang, G.Z.; Luo, X.K.; Huang, Y.H.; Kuang, A.L.; Yuan, H.K.; Chen, H. BiOX/BiOY (X, Y = F, Cl, Br, I) superlattices for visible light photocatalysis applications. *RSC Adv.* **2016**, *6*, 91508–91516. [CrossRef]

54. Long, M.; Hu, P.; Wu, H.; Chen, Y.; Tan, B.; Cai, W. Understanding compositions and electronic structures dependent photocatalytic performance of bismuth oxyiodides. *J. Mater. Chem. A* **2015**, *3*, 5592–5598. [CrossRef]
55. Tian, F.; Zhao, H.P.; Dai, Z.; Cheng, G.; Chen, R. Mediation of valence band maximum of BiOI by Cl incorporation for improved oxidation power in photocatalysis. *Ind. Eng. Chem. Res.* **2016**, *55*, 4969–4978. [CrossRef]